Inactivation of Aβ$_{42}$ Protomer-protomer Dissociation Reaction by Pentamer Dimer Formation

Ikuo Kurisaki[*1], Shigenori Tanaka[*1]

[1]Department of Computational Science, Graduate School of System Informatics, Kobe University, 1-1 Rokkodai-cho, Nada-ku, Kobe 657-8501, Japan

[*]Ikuo Kurisaki

E-mail: kurisaki@bear.kobe-u.ac.jp, Tel: +81-78-803-6472

[*]Shigenori Tanaka

E-mail: tanaka2@kobe-u.ac.jp, Tel: +81-78-803-6620

Abstract

Amyloid fibril growth is supposed to be common pathogenic causes for neurodegenerative diseases, triggered by sufficient amounts of growth nuclei species. Since the molecular entity of growth nuclei is regarded as fibril-like aggregates, clarifying the minimum size of thermodynamically stable fibril-like aggregates has been a long standing problem to understand molecular mechanisms of amyloid fibril growth. We studied this problem by examining relationship between the size of fibril-like amyloid-β (1-42) ($A\beta_{42}$) aggregates and their thermodynamic stability. Seven different protomer dimers were examined as $A\beta_{42}$ fibril-like aggregate models with employing atomistic molecular dynamics simulations. This study has found that increase of protomer size suppresses conformational fluctuation of these aggregates and furthermore inactivates protomer-protomer dissociation reactions by making the reaction timescales much longer than mean lifetime of human beings even at the point of pentamer dimer formation. This observation shows apparent contribution of protomer size to stabilization of fibril-like aggregates and suggests that dimeric form of relatively small protomers such as $A\beta_{42}$ pentamer can function as growth nuclei species, whose accumulation brings about amyloid fibril growth. Meanwhile, $A\beta_{42}$ monomer dissociation from the edges of protomers can occur within timescales ranging from microsecond to second and could

work for $A\beta_{42}$ protomer decomposition. Suppressing the decomposition route may trigger stable $A\beta_{42}$ growth nuclei formation and then promote amyloid fibril growth.

Introduction

Amyloid formation of proteins has been widely observed in biological systems and such aggregate products are classified into the two categories, functional amyloid and pathogenic amyloid.[1] In particular, the latter have drawn much attention because they are supposed as causes of several neurodegenerative diseases, such as Alzheimer and Parkinson diseases.[2]

Since suppression of amyloid formation is considered as practical therapeutic strategy for these serious diseases,[3,4] molecular mechanisms for their formation have been extensively studied.[5-7] It is supposed that amyloid fibril formation proceeds via the consecutive three phases. Firstly, monomers assemble to make repertoire of oligomers; a part of oligomers assumes fibril-like, growth-competent aggregates referred to as growth nuclei (lag phase).[8,9] Secondly, growth nuclei species associate with each other to make larger protofibrils while they convert natively folded monomers into growth-competent monomers to enhance rapid fibril formation (growth phase). Finally, fibril growth processes are balanced with fibril decomposition processes, then reaching thermal equilibrium and completing fibril formation (plateau phase).

In particular, the progress from lag phase to growth phase plays a critical role in an amyloid fibril formation. Sufficient amounts of growth nuclei species are formed in the

lag phase[10], then triggering amyloid fibril growth[9]. The molecular entity of growth nuclei is regarded as fibril-like aggregates.[9] Thus clarifying the minimum size of thermodynamically stable fibril-like aggregates, which can be involved in amyloid fibril growth, is a landmark to understand molecular mechanisms for the shift from lag phase to growth phase, but has still been performed unsatisfactorily.

Then, we address to reach this landmark knowledge by examining the speculation we made in our earlier study[11]: amyloid-β (1-42) ($A\beta_{42}$) protomer growth results in suppression of conformational fluctuation such as inter-$A\beta_{42}$ protomer twisting and then thermodynamically stabilizes $A\beta_{42}$ protofibrils.

Recalling earlier experimental studies on preliminary formation of $A\beta_{42}$ aggregates[12-14], we could find thermodynamically stable, growth-competent aggregates among oligomeric $A\beta_{42}$ species. Meanwhile we should note molecular diversity of $A\beta_{42}$ aggregates appearing in lag phase[15-18]. It is still challenging for experimental approaches to separately examine physicochemical characters of individual oligomeric aggregate species. For the purpose, molecular simulations are practical tools because they can selectively analyze a specific aggregate species.

In this study, we examined relationship between the size of fibril-like $A\beta_{42}$ aggregates and their thermodynamic stability, aiming to identify the minimum species of irreversibly

formed fibril-like $A\beta_{42}$ aggregate within biological period. We performed molecular dynamics simulations for seven $A\beta_{42}$ protomer dimers as models of $A\beta_{42}$ fibril-like aggregates, where sizes of $A\beta_{42}$ protomer range from tetramer to decamer. Conformational fluctuation and dissociation free energies of these dimers were analyzed to validate the relationship.

We then observed inactivation of protomer-protomer dissociation reactions even for $A\beta_{42}$ pentamer dimer. It is noted that $A\beta_{42}$ pentamer is found in the range of size of experimentally-observed soluble $A\beta_{42}$ oligomers[13,19] and such small oligomeric aggregates are supposed to promote amyloid fibril formation by functioning as secondary nucleation competent aggregates[19]. Our observation then suggests that stable formation of this protomer species is a turning point in $A\beta_{42}$ amyloid fibril formation processes, then being worth noting when we consider microscopic mechanisms for shift from the lag phase to the growth phase.

Materials and Methods

Setup of amyloid-β (1-42) protomer dimer systems

We used the cryo-electron microscopy (cryo-EM) structure (PDB entry: 5OQV[20]) to construct amyloid-β (1-42), $A\beta_{42}$, protomer dimer systems; a protomer denotes an $A\beta_{42}$

oligomer composed of $A\beta_{42}$ monomers with growth-competent conformation. Here we consider dimer of *N*-mer $A\beta_{42}$ protomer as the model of fibril-like aggregate, where the value of *N* ranges 4 to 10 (**Figure 1**). Each of the seven models is annotated by $A\beta_{42}$(N:N) or simply N:N, hereafter. Nε protonation state was employed for each of histidine residues, and all carboxyl groups in aspartate and glutamate residues were set to the deprotonated state. Employing each of the seven $A\beta_{42}$(N:N), we prepared seven $A\beta_{42}$ protomer dimer systems, whose annotations and molecular components are summarized in **Table 1**. The additional detail for system construction is described in Supporting Information (see **SI-1**).

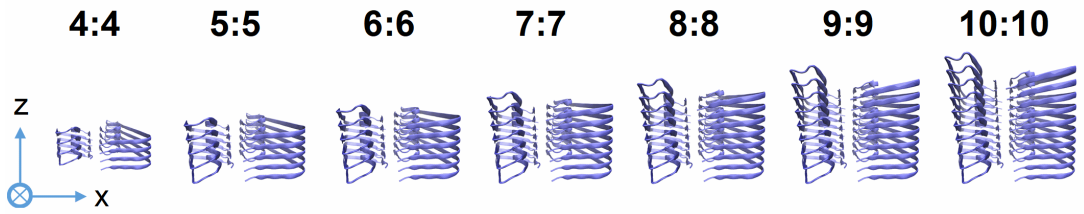

Figure 1. Molecular structures of $A\beta_{42}$ protomer dimers. Each of two integers separated by colon denotes the number of $A\beta_{42}$ monomer in the protomer. The X and Z axes are shown on this plane. The cross in circle denotes Y-axis which directs from this surface to the back.

Table 1. Molecular components of $A\beta_{42}$ protomer dimer systems employed for the molecular dynamics simulations.

size of $A\beta_{42}$ protomer	number of K^+ cations	number of water molecules	box axis length [Å]		
			x	y	z
4	24	33406	138.4	104.2	78.4
5	30	35679	139.1	105.4	83.3
6	36	38153	139.8	106.0	87.7
7	42	41156	140.5	106.9	92.5
8	48	42498	140.6	107.4	96.8
9	54	44855	141.5	108.4	101.7
10	60	46828	141.6	109.2	106.4

To calculate the forces acting among atoms, AMBER force field 14SB[21], TIP3P water model[22,23], and JC ion parameters adjusted for the TIP3P water model[24,25] were used for amino acid residues, water molecules, and ions, respectively. Molecular modeling of each $A\beta_{42}$(N:N) system was performed using the LEaP modules in AmberTools 17 package[26].

Simulation setup

Molecular mechanics (MM) and molecular dynamics (MD) simulations were performed under the periodic boundary condition with GPU-version PMEMD module in AMBER 17 package[26] based on SPFP algorism[27] with NVIDIA GeForce GTX1080 Ti.

Electrostatic interaction was treated by the Particle Mesh Ewald method, where the real space cutoff was set to 9 Å. The vibrational motions associated with hydrogen atoms were frozen by SHAKE algorithm through MD simulations. The translational center-of-mass motion of the whole system was removed by every 500 steps to keep the whole system around the origin, avoiding an overflow of coordinate information from the MD trajectory format. These simulation conditions mentioned above were common in all of the simulations discussed in this manuscript.

Unbiased molecular dynamics simulation

Following temperature relaxation NVT simulations, 30-ns NPT MD simulations (300 K, 1 bar) were performed and used for following analyses. The system temperature and pressure were regulated with Berendsen thermostat[28] with a 5-ps of coupling constant and Monte Carlo barostat with attempt of system volume change by every 100 steps, respectively. A set of initial atomic velocities was randomly assigned from the Maxwellian distribution at 0.001 K at the beginning of the NVT simulations. The time step of integration was set to 2 fs. For each $A\beta_{42}$ fibril system, this simulation procedure was repeated thirty times by assigning different initial atomic velocities. The further details are shown in Supporting Information (see **SI-2**).

Steered and umbrella sampling molecular dynamics simulations

Dissociation processes of $A\beta_{42}$ monomer or $A\beta_{42}$ protomer were described by combining a steered molecular dynamics (SMD) simulation with umbrella sampling molecular dynamics (USMD) simulations. The definitions for reaction coordinates for both SMD and USMD simulations are given in Results and Discussion section.

SMD was employed to dissociate an $A\beta_{42}$ monomer or protomer from the remaining part of $A\beta_{42}$(N:N). 0.25-ns SMD simulation was carried out under constant NPT condition (300 K, 1 bar), where the system temperature and pressure were regulated by Langevin thermostat with 1-ps^{-1} collision coefficient, and Monte Carlo barostat with attempt of system volume change by every 100 steps, respectively. The value of reaction coordinate was gradually changed through the SMD simulations by imposing the harmonic potential with the force constant of 100 kcal/mol/$Å^2$.

Then, certain numbers of snapshot structures were extracted from the SMD trajectory and employed for USMD windows. Following temperature relaxation simulations, several nanosecond NVT USMD simulations (300 K) were performed for each of the USMD windows (**Table S1** and **Tables S2-3** in Supporting Information for $A\beta_{42}$ protomer dissociation and $A\beta_{42}$ monomer dissociation, respectively). The system temperature was

regulated using Langevin thermostat with 1-ps^{-1} collision coefficient. Each of the last 1-ns USMD trajectories was used to construct a potential of mean force.

This combined SMD-USMD procedures are repeated eight times for each $A\beta_{42}$ protomer dimer system. Sets of initial atomic coordinates for SMD simulations were randomly selected from the thirty set of unbiased 30-ns NPT MD simulations without allowing duplication. The further details are illustrated in Supporting Information (see **SI-3**).

Trajectory analyses

Dihedral angle, hydrogen bond (HB) formation and root mean square deviation (RMSd) were calculated with the cpptraj module in AmberTools 17 package[26]. We calculated RMSd to the cryo-EM derived $A\beta_{42}$ protomer dimer structure[20] using the backbone heavy atoms (i.e., C_α, N, C and O). The geometrical criterion of HB formation is as follows: H-X distance was < 3.5 Å and X-H-Y angle was > 120˚, where X, Y and H denote acceptor, donor and hydrogen atoms, respectively.

Each set of USMD trajectories was used to calculate potential of mean force (PMF) with Weighed Histogram Analysis Method (WHAM)[29,30]. Statistical errors of PMF values, $\sigma_{PMF}(\xi)$, were estimated by employing bootstrapped sampling[31]:

$$\sigma_{PMF}(\xi)=\left[(N_b-1)^{-1}\sum_{k=1}^{N_b}\left(W_{b,k}(\xi)-\langle W_b(\xi)\rangle\right)^2\right]^{\frac{1}{2}} \quad (1)$$

Here, N_b, ξ, and $W_{b,k}(\xi)$ denote the number of bootstrapped sampling, the reaction coordinate and the value of kth bootstrapped potential of mean force at each point of ξ, respectively. $\langle W_b(\xi)\rangle$ is average over all $W_{b,k}(\xi)$, where the value of N_b is set to 200.

Reaction rate, k_{TST}, is estimated by using Eyring's transition state theory:

$$k_{TST}=\frac{k_B T}{h}\exp\left(\frac{-\Delta F^{\dagger}}{k_B T}\right) \quad (2)$$

Here, $\Delta F^{\dagger}$, h, k_B and T denote an activation barrier height, Planck constant, Boltzmann constant and a temperature of system, respectively. Reaction time scale, τ_{TST}, is defined as the inverse of k_{TST}. $\Delta F^{\dagger}$ is defined as $F(\xi_0')-F(\xi_0)$, where PMF has local minimum at ξ_0, and gradient of PMF turns from positive to negative values at ξ_0', which is greater than ξ_0. The estimation with employing Eq. 2 is supposed to be an upper bound of the reaction rate (or a lower bound of the reaction time)[32,33] and we accordingly remarked the influence on each of observations we obtained (see related discussion in Results and Discussion section).

Molecular structures were illustrated using Visual Molecular Dynamics (VMD).[34] Error bars are calculated from standard error and indicate 95% confidence interval if there is no annotation.

Results and Discussion

Inter-Aβ_{42} protomer twisting is suppressed through fibril growth

We examined conformational fluctuation of Aβ_{42} protomer dimers under thermal equilibrium by employing each thirty sets of 30-ns unbiased NPT MD simulations. **Figure 2** shows time-course change of averaged RMSd values for Aβ_{42} protomer dimers. Larger protomer dimers have smaller converged RMSd values, suggesting suppression of conformational fluctuation through protofibril growth. For each of the seven systems, it can be considered that the values reach equilibrium after 20 ns. Aβ(4:4) system shows relatively large RMSd fluctuation compared with the other six systems. Nonetheless, the fluctuation is in magnitude of c.a. 0.2 Å within the time domain and seems smaller than atomic scales, then possibly being insignificant. Accordingly, we employed partial MD trajectories in the period after 20 ns for following analyses.

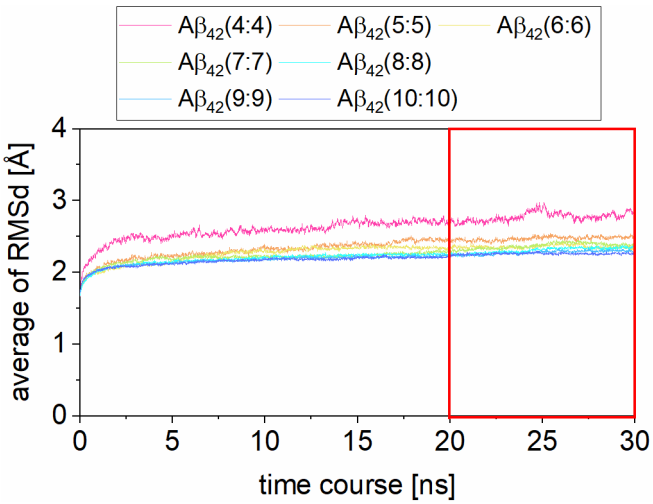

Figure 2. Time-course analyses of root mean square deviation (RMSd). Each result of Aβ42 protomer dimer systems is distinguished by color. The time domain supposed as convergence is indicated by the red rectangle.

We characterize conformational fluctuation of Aβ42 protomer dimer by using the inter-Aβ42 protomer twisting angle (θ_T) (**Figure 3A**). This θ_T is defined as the dihedral angle in the manner similar to that in our earlier study[11]. **Table 2** gives statistical analyses for values of θ_T calculated for each of the seven systems. We could not find significant difference in averaged value of θ_T among the seven systems. Meanwhile, standard deviation (S. D.) reflects the effect of protomer size; Aβ42(4:4) shows larger S. D. of θ_T than the other systems.

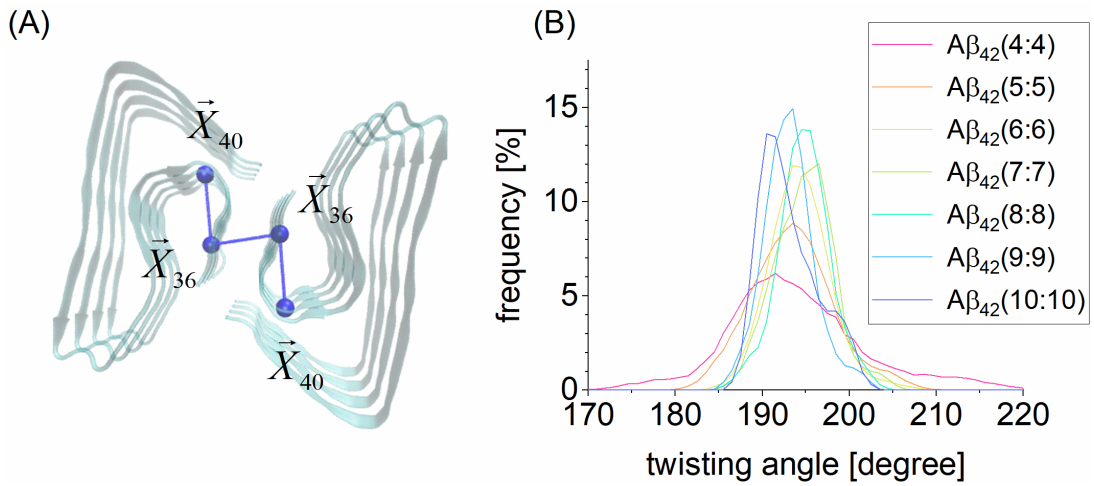

Figure 3. Inter-Aβ42 protomer twisting angle. (A) illustration of the twisting angle. (B) twisting angle distributions for each Aβ42 protomer dimer system. In panel A, $\vec{X}_m$ denotes the coordinate averaged for the Cα atoms of the mth residues in a Aβ42 monomer over the protomer (shown with blue ball); Aβ42(4:4) is illustrated here as an example. In panel B, each result of Aβ42 protomer dimer systems is distinguished by color, and bin width is set to 1˚.

Table 2. Statistical analyses of inter-Aβ42 protomer twisting angle.

Aβ$_{42}$ protofibril model system	twisting angle [deg.]	
	average ± 2 × S. E.*	S. D.*
Aβ$_{42}$(4:4)	193.9 ± 2.6	7.1
Aβ$_{42}$(5:5)	193.5 ± 1.5	4.0
Aβ$_{42}$(6:6)	194.3 ± 1.1	2.9
Aβ$_{42}$(7:7)	194.9 ± 1.1	2.9
Aβ$_{42}$(8:8)	194.8 ± 1.0	2.7
Aβ$_{42}$(9:9)	193.1 ± 1.0	2.7
Aβ$_{42}$(10:10)	193.1 ± 1.2	3.2

*S. E. and S. D. denote standard error and standard deviation, respectively.

Dependence of the S. D. on protomer size can be further clarified by showing the shapes of the distributions of θ_T (**Figure 3B**). That for $A\beta_{42}$(4:4) shows longer tails (the S.D. value is 7.0 [deg.]) than those for other systems. Comparing $A\beta_{42}$(5:5) with $A\beta_{42}$(4:4), the S. D. value shows 1.75-fold decrease, for example. We can find further localization of distributions for larger $A\beta_{42}$ protomer dimers, whose S. D. values are c.a. 3.0 [deg.]. These observations clearly indicate that $A\beta_{42}$ protofibril growth results in suppression of inter-protomer rotation. This result validates the former part of our hypothesis.

Increase of hydrogen bond formation between the protomers additively changes the height of free barrier of protomer dissociation reaction

We test the latter part of our hypothesis that suppressing conformational fluctuation of $A\beta_{42}$ protomer dimer actually enhances thermodynamic stability of the protomer dimer. A potential of mean force (PMF) was calculated for each of protomer-protomer dissociation reactions, where the distance between centers of mass for each protomer is employed as the reaction coordinates (see **Figure 4A** for the definition).

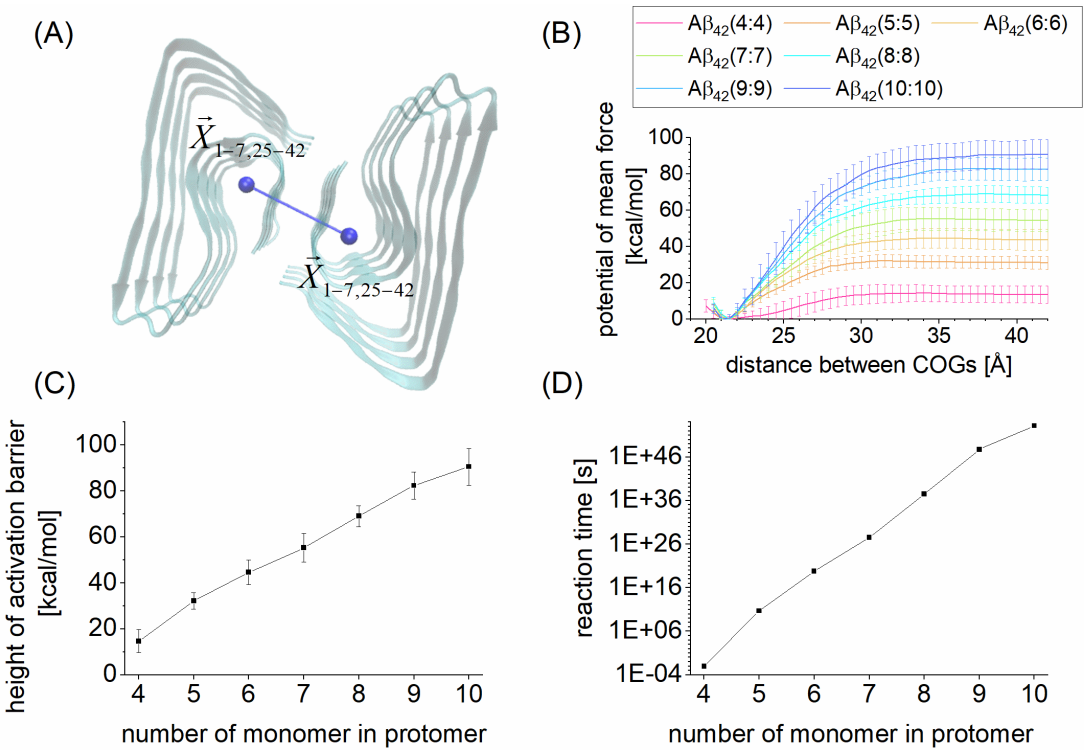

Figure 4. Analyses for Aβ42 protomer-protomer dissociation reaction. (A) Illustration of reaction coordinate. (B) Potential of mean forces (PMFs). (C) Height of activation barrier obtained from the PMFs. (D) Reaction time evaluated with Erying's transition state theory. In panel A, $\vec{X}_{m-n,s-t}$ denotes the averaged coordinate (shown with blue ball), which is calculated for the (n−m+1) Cα atoms of the mth, $m+1^{th}$ … n^{th} and s^{th}, $s+1^{th}$ … t^{th} residues in the protomer, and the case of Aβ42(4:4) is illustrated here as an example. In panel B, each of Aβ42 protomer dimer systems is distinguished by color.

As shown in **Figure 4B**, each of the PMFs has one activation barrier toward the dissociation direction, appearing to be uphill. Furthermore, the height of activation barrier clearly increases with the size of protomer, thus corroborating the latter part of our

hypothesis (**Figure 4C**).

This change can be explained by considering the number of hydrogen bond (HB) formation between the protomers. **Figure 4C** and **Figure 5A** show the height of activation barrier and the number of inter-Aβ_{42} protomer HB, respectively. We can find that both of these two quantities additively change according to protomer size and it thus could be said that increase of the protomer size directly contributes to enthalpic stabilization of Aβ_{42} protomer dimers and suppresses inter-protomer rotation.

It is worthwhile to note that the number of hydrogen bond formation per Aβ_{42} monomer ($n_{monomer}^{HB}$) seems to converge up to Aβ_{42}(8:8) (**Figure 5B**): $n_{monomer}^{HB}$ shows monomer size-dependent, *extensive* property by Aβ_{42}(7:7), while it converts into monomer size-independent *intensive* variable from Aβ_{42}(8:8). This observation let us suggest that Aβ_{42}(8:8) is a boundary where a flexible fibril-like aggregate converts into solid Aβ_{42} protofibril structure.

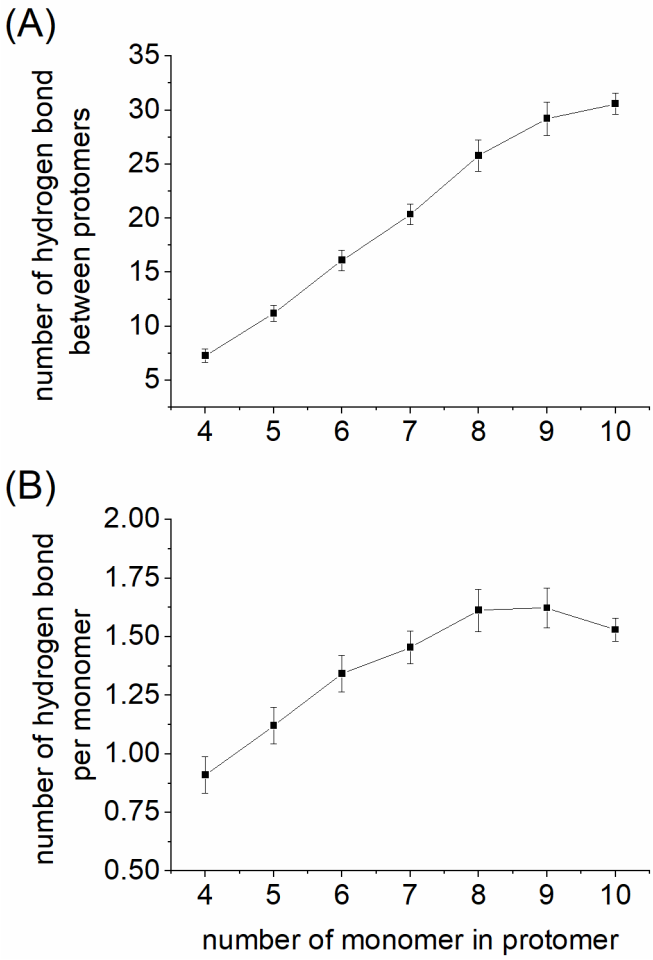

Figure 5. Hydrogen bond (HB) formation between Aβ$_{42}$ protomers. (A) whole number of the HB. (B) the number of HB divided by the number of Aβ$_{42}$ monomer in the Aβ$_{42}$ protomer dimer.

Using the heights of activation barriers calculated above, we estimated the time scale of protomer dissociation reactions (τ [s]) (**Figure 4D**). From the biological point of view, it is worthwhile discussing the difference between that of Aβ$_{42}$(4:4) and Aβ$_{42}$(5:5), in particular. According to our estimations with Eyring's transition state theory, the value of τ for Aβ$_{42}$(4:4) is 8.8 ms which falls into timescales of cellular processes, while that for

$A\beta_{42}$(5:5) is 1680 year which is much longer than mean lifetime of human being. This reaction time estimation denotes that the protomer-protomer dissociation reaction is kinetically inactivated in decomposition processes of $A\beta_{42}$(5:5) and also in those of greater protomer dimers.

Since Eyring's transition state theory would often underestimate reaction timescales,[32,33] correction of such underestimation might indicate that oligomeric species smaller than $A\beta_{42}$(5:5), *e.g.*, $A\beta_{42}$(4:4), show inactivation of inter-protomer dissociation as well. Nonetheless, the observation results for inactivation of inter-$A\beta_{42}$ protomer dissociation within mean lifetime of human being would remain unchanged essentially.

The above insight, which is obtained by considering the seven model systems of $A\beta_{42}$ fibril-like aggregate, supports our speculation that increasing size of protomer contributes to thermodynamic stability of fibril-like aggregates. Furthermore, inactivation of protomer-protomer dissociation route is found for relatively small protomer dimer, $A\beta_{42}$(5:5).

The recent experimental studies reported that the number of subunits in soluble $A\beta_{42}$ aggregates ranges from 4 to 9[13,19]. Besides, such smaller oligomer species are supposed to be secondary nucleation competent aggregates which can convert natively folded monomers into growth-competent monomers.[19] Recalling these two experimental

observations, we could suppose that stable formation of fibril-like $A\beta_{42}$ pentamer species, which probably activates secondary nucleation processes, generates additional fibril-like oligomers and accumulate growth nuclei species via dimeric association of this protomer species, is an important turning point where the growth phase proceeds from the lag phase.

$A\beta_{42}$ protomer size has lesser influence on monomer dissociation from the edge of a protomer dimer

It can be assumed that increase of protomer size similarly excludes an alternative route of $A\beta_{42}$ aggregate decomposition, that is, $A\beta_{42}$ monomer dissociation from the edges of protomers. To examine effects of protomer size on the alternative dissociation route, we analyzed thermodynamic stability of $A\beta_{42}$ monomer on the protomer edge. We calculated potential of mean forces for monomer dissociations from $A\beta_{42}$(4:4) and $A\beta_{42}$(10:10) (**Figure 6A** and **6B**), the smallest and largest protomer dimers examined in this study, respectively.

The estimated reaction times are 1.6 μs and 5.9 ms for $A\beta_{42}$(4:4) and $A\beta_{42}$(10:10), respectively. Although increase of protomer size leads to suppression of monomer dissociation from a protomer edge, the estimated reaction time is still within several milli seconds even for $A\beta_{42}$(10:10). Then, monomer dissociation reaction from the $A\beta_{42}$(4:4)

edges may work for an active route of $A\beta_{42}$(4:4) protomer dimer decomposition.

It is noted that Eyring's transition state theory would often underestimate the reaction time[32,33], while the above observation is unchanged essentially. Referring to earlier kinetic studies on other biomacromolecular processes[35-37], their underestimation corrections ranges from 10^1- to 10^6-fold, which depends on the molecular processes they studied. Nonetheless, even if we consider the largest correction, 10^6-fold larger value for monomer dissociation from $A\beta_{42}$(4:4) edges, the value of 1.6 s still falls into timescales of cellular processes. It could be then supposed that $A\beta_{42}$ monomer dissociation is an active route for decomposition of $A\beta_{42}$ protomer in the dimeric form even under inactivation of protomer-protomer dissociation.

Although it is still uncertain so far that stable formation of oligomeric protomers such as $A\beta_{42}$ pentamer is actually prevented by $A\beta_{42}$ monomer dissociation from $A\beta_{42}$ protomer edges, it is worthwhile noting the possibility that this reaction route works against growth nuclei formation. The earlier studies reported fibril-like aggregate formation accompanied by the molecular crowding of $A\beta_{42}$ molecules[12,14,38]. This experimental observation lets us evoke such a scenario that $A\beta_{42}$ monomer dissociation reaction works to decompose oligomeric $A\beta_{42}$ protomers isolated in aqueous solution while the decomposition process is suppressed by crowding of $A\beta_{42}$ species surrounding $A\beta_{42}$

protomers, which enhances (re)binding of Aβ42 monomers to Aβ42 protomers. Nonetheless, further investigation for effects of the reaction route and Aβ42 crowding on growth nuclei formation is beyond the scope of this study, thus being left for future study.

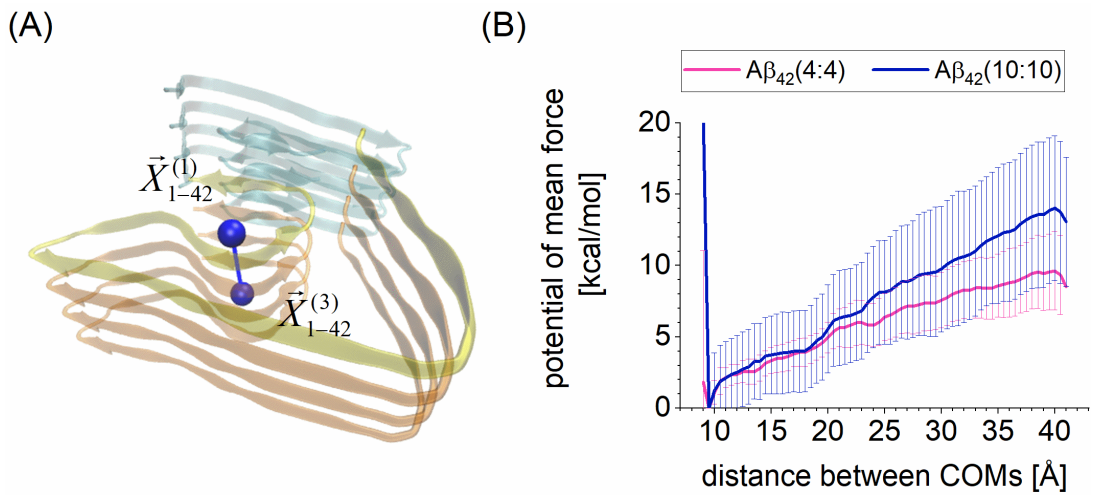

Figure 6. Analyses for Aβ42 monomer dissociation reaction. (A) Illustration of reaction coordinate. (B) Potential of mean forces (PMFs). In panel A, $\vec{X}^{(l)}_{m-n}$ denotes the averaged coordinate (shown with blue ball), which is calculated for the (n−m+1) Cα atoms of the mth, m+1th … n^{th} residues for l monomers in the protomer, and the case of Aβ42(4:4) is illustrated here as an example. The dissociated monomer and the neighboring trimer is colored by transparent yellow and blue, respectively. In panel B, each of Aβ42 protofibril systems is distinguished by color.

Concluding Remarks

Clarifying minimum size of growth-competent aggregates is a landmark knowledge to

understand molecular mechanisms for amyloid fibril formation. In this context, we considered a paradigmatic amyloid protein, $A\beta_{42}$, and examined relationship between the protomer size and thermodynamic stability of the protomer dimers. We elucidated that even dimer formation of $A\beta_{42}$ pentamer kinetically inactivates this protomer-protomer dissociation within lifetime of human being.

Our observation about $A\beta_{42}$ pentamer dimer appears to be worth noting when we examine how the growth phase proceeds from the lag phase. $A\beta_{42}$ pentamer is found in the range of size of experimentally-observed soluble $A\beta_{42}$ oligomers[13,19], which are supposed to be secondary nucleation competent aggregates[19]. Recalling these experimental observations, we could suppose that stable formation of $A\beta_{42}$ pentamer activates secondary nucleation processes, generates additional fibril-like oligomers and accumulate growth nuclei species through dimeric association of this protomer species, then leading to amyloid fibril formation.

We have here discussed $A\beta_{42}$ protomer systems, while our theoretical approach can be applicable to other pathogenic amyloid proteins such as prion[39], α-synuclein[40] and fused in sarcoma (FUS)[41]. Free energy analyses for these proteins could give a similar observation that dimeric association of oligomeric protomer species is sufficient to inactivate protomer-protomer dissociation route in the decomposition process.

Meanwhile it can be assumed that each amyloid protein shows its characteristic protomer size due to the own atomic structure of amyloid-like aggregate.

On the other hand, monomer dissociation routes appear to be still active for decomposition of oligomeric $A\beta_{42}$ protomer. This observation implies an alternative key factor for stable formation of $A\beta_{42}$ growth nuclei species. Recalling the earlier experimental insights into micelle-like aggregate formation upon amyloid fibril growth[12, 14,38], $A\beta_{42}$ molecules crowding around fibril-like aggregates is a possible factor to suppress relatively rapid monomer dissociation routes. This speculation will be examined in future study by considering roles of molecular crowding in stable formation of relatively small protomer dimer such as $A\beta_{42}$(5:5) as model of growth nuclei species.

Supporting Information

The Supporting Information is available free of charge on the ACS Publications website. Detailed procedures for unbiased MD, SMD and USMD simulations, Figures and Tables for analyses of these simulations.

Accession Codes

Amyloid-β(1-42) ($A\beta_{42}$) corresponds to the residues 672-713 of the human amyloid-β precursor protein (UniProt KB P05067).

Acknowledgements

This work was supported by a Grant-Aid for Scientific Research on Innovative Areas "Chemistry for Multimolecular Crowding Biosystems" (JSPS KAKENHI Grand No. JP17H06353).

Author Information

Corresponding Authors

Ikuo Kurisaki - Graduate School of System Informatics, Kobe University, 1-1 Rokkodai, Nada-ku, Kobe 657-8501, Japan; ORCID: 0000-0003-4519-1093; Email:

kurisaki@bear.kobe-u.ac.jp

Shgenori Tanaka - Graduate School of System Informatics, Kobe University, 1-1 Rokkodai, Nada-ku, Kobe 657-8501, Japan; ORCID: 0000-0002-6659-2788; Email: tanaka2@kobe-u.ac.jp

Notes

The authors declare no competing financial interest.

References

1. Chiti, F.; Dobson, C. M., Protein Misfolding, Amyloid Formation, and Human Disease: A Summary of Progress Over The Last Decade. *Annu. Rev.Biochem.* **2017**, *86*, 27-68.

2. Chiti, F.; Dobson, C. M., Protein Misfolding, Functional Amyloid, and Human Disease. *Ann. Rev. Biochem.* **2006**, *75*, 333-366.

3. Tolar, M.; Abushakra, S.; Sabbagh, M., The Path Forward in Alzheimer's Disease Therapeutics: Reevaluating the Amyloid Cascade Hypothesis. *Alzheimers Dement.* **2020**, *16*, 1553-1560.

4. Selkoe, D. J.; Hardy, J., The Amyloid Hypothesis of Alzheimer's Disease at 25 Years. *Embo Mol. Med.* **2016**, *8*, 595-608.

5. Knowles, T. P. J.; Waudby, C. A.; Devlin, G. L.; Cohen, S. I. A.; Aguzzi, A.; Vendruscolo, M.; Terentjev, E. M.; Welland, M. E.; Dobson, C. M., An Analytical Solution to the Kinetics of Breakable Filament Assembly. *Science* **2009**, *326*, 1533-1537.

6. Cohen, S. I. A.; Linse, S.; Luheshi, L. M.; Hellstrand, E.; White, D. A.; Rajah, L.; Otzen, D. E.; Vendruscolo, M.; Dobson, C. M.; Knowles, T. P. J., Proliferation of Amyloid-β 42 Aggregates Occurs through A Secondary Nucleation Mechanism. *P. Natl. Acad. Sci. USA* **2013**, *110*, 9758-9763.

7. Owen, M. C.; Gnutt, D.; Gao, M. M.; Warmlander, S. K. T. S.; Jarvet, J.; Graslund, A.; Winter, R.; Ebbinghaus, S.; Strodel, B., Effects of In Vivo Conditions on Amyloid Aggregation. *Chem. Soc. Rev.* **2019**, *48*, 3946-3996.

8. Harper, J. D.; Lansbury, P. T., Models of Amyloid Seeding in Alzheimier's Disease and Scrapie: Mechanistic Truths and Physiological Consequences of the Time-dependent Solubility of Amyloid Proteins. *Annu. Rev. Biochem.* **1997**, *66*, 385-407.

9. Ruggeri, F. S.; Sneideris, T.; Vendruscolo, M.; Knowles, T. P. J., Atomic Force Microscopy for Single Molecule Characterisation of Protein Aggregation. *Arch. Biochem. Biophys.* **2019**, *664*, 134-148.

10. Cohen, S. I. A.; Vendruscolo, M.; Dobson, C. M.; Knowles, T. P. J., From Macroscopic Measurements to Microscopic Mechanisms of Protein Aggregation. *J. Mol. Biol.* **2012**, *421*, 160-171.

11. Kurisaki, I.; Tanaka, S., ATP Converts Aβ(42) Oligomer into Off-Pathway Species by Making Contact with Its Backbone Atoms Using Hydrophobic Adenosine. *J Phys Chem B* **2019**, *123*, 9922-9933.

12. Sabate, R.; Estelrich, J., Evidence of The Existence of Micelles in The Fibrillogenesis of β-amyloid Peptide. *J. Phys. Chem. B* **2005**, *109*, 11027-11032.

13. Wolff, M.; Zhang-Haagen, B.; Decker, C.; Barz, B.; Schneider, M.; Biehl, R.;

Radulescu, A.; Strodel, B.; Willbold, D.; Nagel-Steger, L., Aβ_{42} Pentamers/Hexamers Are the Smallest Detectable Oligomers in Solution. *Sci. Rep,-Uk* **2017**, *7*. https://doi.org/10.1038/s41598-017-02370-3

14. Novo, M.; Freire, S.; Al-Soufi, W., Critical Aggregation Concentration for The Formation of Early Amyloid-β (1-42) Oligomers. *Sci Rep-Uk* **2018**, *8*. https://doi.org/10.1038/s41598-018-19961-3

15. Colletier, J. P.; Laganowsky, A.; Landau, M.; Zhao, M.; Soriaga, A. B.; Goldschmidt, L.; Flot, D.; Cascio, D.; Sawaya, M. R.; Eisenberg, D., Molecular Basis for Amyloid-β Polymorphism. *Proc. Natl. Acad. Sci. U S A* **2011**, *108*, 16938-43.

16. Hard, T., Protein Engineering to Stabilize Soluble Amyloid β-protein Aggregates for Structural and Functional Studies. *Febs J.* **2011**, *278*, 3884-3892.

17. De, S.; Wirthensohn, D. C.; Flagmeier, P.; Hughes, C.; Aprile, F. A.; Ruggeri, F. S.; Whiten, D. R.; Emin, D.; Xia, Z. J.; Varela, J. A.; Sormanni, P.; Kundel, F.; Knowles, T. P. J.; Dobson, C. M.; Bryant, C.; Vendruscolo, M.; Klenerman, D., Different Soluble Aggregates of Aβ42 Can Give Rise to Cellular Toxicity Through Different Mechanisms. *Nat. Commun.* **2019**, *10*. https://doi.org/10.1038/s41467-019-09477-3

18. Kollmer, M.; Close, W.; Funk, L.; Rasmussen, J.; Bsoul, A.; Schierhorn, A.; Schmidt, M.; Sigurdson, C. J.; Jucker, M.; Fandrich, M., Cryo-EM Structure and

Polymorphism of Aβ Amyloid Fibrils Purified from Alzheimer's Brain Tissue. *Nat. Commun.* **2019**, *10*. https://doi.org/10.1038/s41467-019-12683-8

19. Leppert, A.; Tiiman, A.; Kronqvist, N.; Landreh, M.; Abelein, A.; Vukojević, V.; Johansson, J., Smallest Secondary Nucleation Competent Aβ Aggregates Probed by an ATP-Independent Molecular Chaperone Domain. *Biochemistry* **2021**, *60*, 678-688.

20. Gremer, L.; Scholzel, D.; Schenk, C.; Reinartz, E.; Labahn, J.; Ravelli, R. B. G.; Tusche, M.; Lopez-Iglesias, C.; Hoyer, W.; Heise, H.; Willbold, D.; Schroder, G. F., Fibril Structure of Amyloid-β(1-42) by Cryo-electron Microscopy. *Science* **2017**, *358*, 116-119.

21. Maier, J. A.; Martinez, C.; Kasavajhala, K.; Wickstrom, L.; Hauser, K. E.; Simmerling, C., ff14SB: Improving the Accuracy of Protein Side Chain and Backbone Parameters from ff99SB. *J. Chem. Theory Comput.* **2015**, *11*, 3696-3713.

22. Jorgensen, W. L.; Chandrasekhar, J.; Madura, J. D.; Impey, R. W.; Klein, M. L., Comparison of Simple Potential Functions for Simulating Liquid Water. *J. Chem. Phys.* **1983**, *79*, 926-935.

23. Kusalik, P. G.; Svishchev, I. M., The Spatial Structure in Liquid Water. *Science* **1994**, *265*, 1219-1221.

24. Joung, I. S.; Cheatham, T. E., Determination of Alkali and Halide Monovalent Ion Parameters for Use in Explicitly Solvated Biomolecular Simulations. *J. Phys. Chem.*

B **2008**, *112*, 9020-9041.

25. Joung, I. S.; Cheatham, T. E., III, Molecular Dynamics Simulations of the Dynamic and Energetic Properties of Alkali and Halide Ions Using Water-Model-Specific Ion Parameters. *J. Phys. Chem. B* **2009**, *113*, 13279-13290.

26. Case, D. A.; Cerutti, D. S.; Cheatham, T. E., III ; Darden, T. A.; Duke, R. E.; Giese, T. J.; Gohlke, H.; Goetz, A. W.; Greene, D.; Homeyer, N.; Izadi, S.; Kovalenko, A.; Lee, T. S.; LeGrand, S.; Li, P.; Lin, C.; Liu, J.; Luchko, T.; Luo, R.; Mermelstein, D.; Merz, K. M.; Monard, G.; Nguyen, H.; Omelyan, I.; Onufriev, A.; Pan, F.; Qi, R.; Roe, D. R.; Roitberg, A.; Sagui, C.; Simmerling, C.; Botello-Smith, W. M.; Swails, J.; Walker, R. C.; Wang, J.; Wolf, R. M.; Wu, X.; Xiao, L.; York, D. M.; Kollman, P. A. *Amber 17*; University of California: San Francisco, CA, 2017.

27. Le Grand, S.; Gotz, A. W.; Walker, R. C., SPFP: Speed without Compromise-A Mixed Precision Dodel for GPU Accelerated Molecular Dynamics Simulations. *Comput. Phys. Commun.* **2013**, *184*, 374-380.

28. Berendsen, H. J. C.; Postma, J. P. M.; Vangunsteren, W. F.; Dinola, A.; Haak, J. R., Molecular-dynamics with Couping to An External Bath. *J. Chem. Phys.* **1984**, *81*, 3684-3690.

29. Grossfield , A. *WHAM: the Weighted Histogram Analysis Method*, version 2.0.9;

University of Rochester Medical Center: Rochester, NY, 2013.

30. Kumar, S.; Bouzida, D.; Swendsen, R. H.; Kollman, P. A.; Rosenberg, J. M., The Weighted Histogram Analysis Method for Free-Energy Calculations on Biomolecules .1. The Method. *J. Comput. Chem.* **1992**, *13*, 1011-1021.

31. Hub, J. S.; de Groot, B. L.; van der Spoel, D., g_wham-A Free Weighted Histogram Analysis Implementation Including Robust Error and Autocorrelation Estimates. *J. Chem. Theory Comput.* **2010**, *6*, 3713-3720.

32. Case, D. A., Dynamical Simulation of Rate Constants in Protein-Ligand Interactions. *Prog Biophys Mol Bio* **1988**, *52* (1), 39-70.

33. Zhou, H. X., Rate Theories for Biologists. *Q. Rev. Biophys.* **2010**, *43*, 219-293.

34. Humphrey, W.; Dalke, A.; Schulten, K., VMD: Visual Molecular Dynamics. *J. Mol. Graphics Modell.* **1996**, *14*, 33-38.

35. Roux, B.; Karplus, M., Ion-Transport in a Gramicidin-Like Channel - Dynamics and Mobility. *J. Phys. Chem.* **1991**, *95*, 4856-4868.

36. Hridya, V. M.; Hynes, J. T.; Mukherjee, A., Dynamical Recrossing in the Intercalation Process of the Anticancer Agent Proflavine into DNA. *J. Phys. Chem. B* **2019**, *123*, 10904-10914.

37. Dutzler, R.; Schirmer, T.; Karplus, M.; Fischer, S., Translocation Mechanism of

Long Sugar Chains across The Maltoporin Membrane Channel. *Structure* **2002**, *10*, 1273-1284.

38. Lomakin, A.; Chung, D. S.; Benedek, G. B.; Kirschner, D. A.; Teplow, D. B., On The Nucleation and Growth of Amyloid β-protein Fibrils: Detection of Nuclei and Quantitation of Rate Constants. *P. Natl. Acad. Sci. USA* **1996**, *93*, 1125-1129.

39. Glynn, C.; Sawaya, M. R.; Ge, P.; Gallagher-Jones, M.; Short, C. W.; Bowman, R.; Apostol, M.; Zhou, Z. H.; Eisenberg, D. S.; Rodriguez, J. A., Cryo-EM Structure of A Human Prion Fibril with A Hydrophobic, Protease-resistant Core. *Nat. Struct. Mol. Biol.* **2020**, *27*, 417-423.

40. Tuttle, M. D.; Comellas, G.; Nieuwkoop, A. J.; Covell, D. J.; Berthold, D. A.; Kloepper, K. D.; Courtney, J. M.; Kim, J. K.; Barclay, A. M.; Kendall, A.; Wan, W.; Stubbs, G.; Schwieters, C. D.; Lee, V. M. Y.; George, J. M.; Rienstra, C. M., Solid-state NMR Structure of A Pathogenic Fibril of Full-length Human Alpha-synuclein. *Nat. Struct. Mol. Biol.* **2016**, *23*, 409-415.

41. Murray, D. T.; Kato, M.; Lin, Y.; Thurber, K. R.; Hung, I.; McKnight, S. L.; Tycko, R., Structure of FUS Protein Fibrils and Its Relevance to Self-Assembly and Phase Separation of Low-Complexity Domains. *Cell* **2017**, *171*, 615-627.e16.
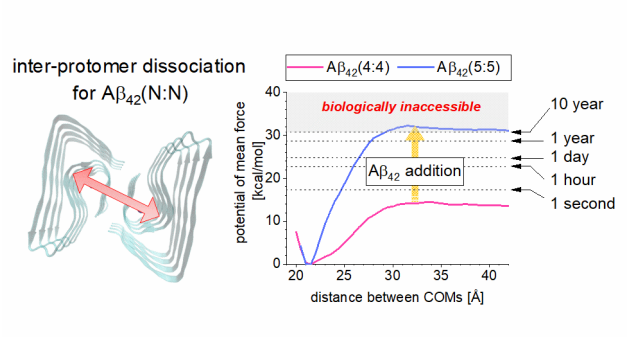
For TOC graphics only